Structural and electronic changes in graphite fluorides as a function of fluorination rate: An XRS, PDF and DFT study

C. Cavallari, M. Brunelli, S. Radescu, M. Dubois, N. Batisse, M. Vaughan, H.E. Fischer, V. Pischedda

Structural and electronic changes in graphite fluorides as a function of fluorination rate: an XRS, PDF and DFT study

C. Cavallari[1*], M.Brunelli [2], S. Radescu[3], M. Dubois[4], N. Batisse[4], G.B.M. Vaughan [1], H. E. Fischer [5] and V. Pischedda[6*]

[1] *ESRF- The European Synchrotron Radiation Facility, 38042 Grenoble cedex, France.*
[2] *Dutch-Belgian Beamline DUBBLE at the ESRF, Grenoble cedex, France.*
[3] *Departamento de Física, Instituto de Materiales y Nanotecnología, MALTA Consolider Team, Universidad de La Laguna, La Laguna, E-38205 Tenerife, Spain*
[4] *Université Clermont Auvergne, Sigma Clermont CNRS, ICCF, UMR CNRS 6296, 24 Avenue Blaise Pascal, 63178, Aubiére, France*
[5] *ILL-Institut Laue Langevin, 38043 Grenoble cedex, France.*
[6] *Institut Lumière Matière, UMR5306 Université Lyon 1-CNRS, Université de Lyon 69622 Villeurbanne cedex, France.*

Abstract

In the present paper, graphite fluoride compounds C_xF with various degrees of fluorination (x = 4, 2 and 1), i.e., with different C-F bonding characteristics, were systematically investigated using X-ray Raman Spectroscopy (XRS) and X-ray and neutron diffraction by means of Pair Distribution Function (PDF) analysis. For both techniques, *ab-initio* calculations allow the experimental results and structural/bonding assignments to be explained and/or confirmed. Presented here for the three stoichiometries are results for the carbon and fluorine first-neighbour distances, the evolution of the electronic band structure due to the change of the carbon hybridization upon fluorination, and also the nature of the final states for 1s core-electron excitations. Since fluorination is limited by the diffusion of fluorine in the carbon lattice, the process is less effective in the bulk, where a graphitic core remains. The cross-checked XRS, PDF data and Density Functional Theory (DFT) simulations appear also to be a powerful method to highlight the presence of a residual graphitic core, even at the highest fluorine content, in such semi-disordered and structurally complex compounds.

*Corresponding authors: Tel: +33476882297 email: chiara.cavallari@esrf.fr (Chiara Cavallari)
Tel: +33472431402 email: vittoria.pischedda@univ-lyon1.fr (Vittoria   Pischedda)

1

1. Introduction

Graphite fluorides C_xF, are fluorine-graphite compounds presenting covalent ($x \leq 2$) or semi-covalent ($x > 2$) C-F bonds, depending on the fluorine content and the synthesis conditions. They exhibit excellent tribological and electrochemical properties and therefore are used in industry as solid lubricants or as cathode in primary lithium batteries [1–3]. The discharge potential and capacity in primary lithium battery can be controlled by fluorine concentration; for example it has been found that sub-fluorinated $CF_{0.78}$ has a powder density 14 times higher than that of the typical Li/CF_1 battery [3,4]. The presence of non-fluorinated graphitic carbons allows the electron flux to be ensured in the insulating CF_x active material. Good performances of C_xF as solid lubricants are also related to the presence of sp^2 carbons, in particular: i) low friction coefficients are observed for intermediate fluorine contents [5] and ii) a defluorination process is observed during the tribofilm formation [6]. Clearly, a deep investigation of the graphite phase distribution into the fluorocarbon matrix of C_xF is of primary importance.

The fine tuning of graphite content, F concentration and C-F bonding allows adjusting the applicative properties such as chemical and thermal stability, tribological properties and the discharge potentials (the stronger the C-F bond, the lower the potential). For these reasons, there has been much interest in the last decades and many discussions in literature to clarify the structure of C_xF compounds and the nature of C-F bonding as well as the repartition of remaining sp^2 carbon atoms. However, as it has not been possible until now to synthesize a homogenous and perfectly crystalline sample, it is difficult experimentally to clarify the crystal structure and a large variety of techniques have been applied to characterize these materials such as XRD, infra-red, optical Raman, XAS, NMR and many others [7–12]. Theoretical studies suggest also a variety of possible structural models for each C_xF compound [13–15].

Several studies established that at low concentration of fluorine, correlated with a low treatment temperature, it is possible to preserve a graphitic structure, with mainly intercalated fluoride ions. This is the case of C_4F in which the hybridization of the carbon atoms remains sp^2 as in the case of graphite. At lower value of x, that is higher fluorine content, as for C_2F and CF, the structure corrugates; the C atoms become mainly hybridized sp^3, as in the diamond structure, with the presence of out of plane C-F bonds [10,12]. The nature of C-F bonds, covalent for intermediate and higher fluorine contents (C_2F and C_1F) and weakened covalence for low concentration (as C_4F) was estimated by NMR, EPR and XAS techniques

[8,11,12,16]. The origin of the weakened covalence (also called semi-covalence) is due to hyperconjugation, i.e. the electrons involved in the C-F covalent bonds are delocalized by the presence of out of plane p_z orbitals from the graphitic planes due to the coexistence of conjugated C=C double bonds in non-fluorinated parts and covalent C–F bonds in fluorocarbon parts [10].

In previous works by *in-situ* high pressure Raman spectroscopy, XRD and *ab-initio* calculations we investigated the structural, vibrational and electronic behavior of C_2F and C_4F at ambient conditions and high pressure exploring the sp^2-sp^3 carbon transition upon fluorination and physical compression [13,14]. Density functional theory (DFT) calculations showed that the coverage of the graphene layer by fluorine is more stable in a single-sided fluorinated configuration (where all the F atoms bind on one side of the graphene layer), while the C_2F structure has a complex mixed sp^2-sp^3 character where graphene layers are intercalated among sp^3 carbon hybridized structural domains. However, the models do not take into account structural, chemical and core-surface inhomogeneity observed in the experimental data. Raman spectroscopy and XRD data clearly indicate the presence of disorder, meaning that conventional approach based on Bragg diffraction is not well adapted for structural studies of these compounds.

In this paper, we investigate the C-F bonding nature of graphite fluorides with different fluorine concentrations C_4F, C_2F and C_1F using two techniques, which, to the best of our knowledge, have never been used before for characterizing these materials: X-ray Raman Scattering (XRS) and Pair Distribution Function (PDF) analysis. These are both bulk techniques very sensitive to the atomic local and electronic structure and C hybridization. PDF is a well-established technique for studying disordered or semi-ordered materials. XRS is a non-resonant inelastic X-ray scattering technique that allows observing the core electron excitations in the sample, thus providing information about the C-F bonding character and the hybridization of the C states [17–20]. Compared to other techniques such as XPS and soft-XAS, that allow obtaining similar information, XRS has the great advantage that the penetration depth of the hard X-ray beam in the sample is of the order of hundreds of micrometers (compared to few nanometers or few hundreds nanometers for XPS and XAS, respectively). This bulk sensitivity is important for the study of graphite fluorides that often present core-surface heterogeneity, the fluorination process being limited by the diffusion of fluorine into the carbon lattice. DFT calculations allow data interpretation to be verified and validated**.**

2. Experimental

2.1. Sample preparation

Graphite fluorides at different levels of fluorination were measured: C_4F, C_2F and C_1F. Sample preparation proceeded via treatment in fluorine gas of graphite powder used as a precursor. More details about the synthesis and fluorination process of the samples are reported in [8, 9, 11, 16]. Pristine graphite powder was natural sample from Madagascar (grain size 75 μm), supplied by Mersen. Graphite and diamond powders were measured as references.

2.2. Characterization

2.2.1 Pair Distribution Function analysis

XRD data for real space analysis were collected at the ID15A beamline (ESRF, Grenoble, France), selecting an energy of E = 65.35 keV (λ = 0.18971 Å), of the incoming beam. Using a Pilatus CdTe detector, a 2D detector system and placing the samples to a sample-to-detector distance of 12.05 cm, a maximum momentum transfer $Q = 4\pi \sin \theta/\lambda$ of $Q_{max} \sim 35$ Å^{-1} was reached. Power samples of C_4F, C_2F, CF and graphite were loaded into 1.5 mm diameter kapton tubes. 64 images of 10 s each were collected (for a total data collection time of about 10 minutes). Data on empty tube was also collected to obtain sufficient statistics for background subtraction. Sample spinning was used to increase powder averaging. Data collected on a CeO_2 powder sample were used for geometrical calibration (7 images of 10 s). Background was systematically subtracted on the raw images before azimuthal integration (using in-house software).

In this work, the PDF is described with the G(r) formalism [21], which indicates the probability of finding a pair of atoms separated by a distance r. G(r) is experimentally determined via sine Fourier transform of the total scattering function $F(Q)$:

$$G(r) = \frac{2}{\pi} \int_0^\infty F(Q) \sin(Qr)\, dQ$$

where Q is the magnitude of the scattering vector, $Q = 4\pi \sin \theta/\lambda$, and r is the interatomic distance. S(Q) is the experimental coherent X-ray scattering intensity, after correcting the raw data for sample self-absorption, multiple and Compton scattering.

Data integration was performed using pyFAI [22] and extraction of the G(r) functions was performed using PDFGetX3 software [23], employing data for the Fourier Transformation to a $Q_{max} = 35$ Å^{-1}.

Neutron powder diffraction (NPD) data [24] for real space analysis were collected at the D4C instrument (ILL, Grenoble, France) [25] at an incident neutron wavelength $\lambda = 0.4964(5)$ Å, covering a Q-range between 0.35 and 23.5 Å^{-1}. Powder samples were placed inside a sealed 7 mm diameter Vanadium cylindrical cell and measured under ambient temperature and vacuum conditions.Vanadium rod, empty cans and boron powder patterns were also measured in order to properly subtract the background and normalize the data. Backgrounds were measured periodically during the experiment in order to assess their stability. PDFs from NPD data were obtained using the standard Placzek correction and Fourier transform, implemented into a software procedure developed at the D4C instrument [26]. In particular, an appropriated background, taking into account a linear combination of the diffraction data for the empty bell jar and empty can and Placzek corrections, was subtracted from the raw data. In addition, multiple scattering and absorption corrections were made using the *CORRECT* program [27]. Resolution of the PDF (i.e. shorter distances which can be distinguished) in the real space covered by the X-ray and the neutron experiments was $\delta r \sim 0.1 \div 0.16$ Å, respectively.

2.2.2 X-ray Raman scattering

All XRS data were collected using the large solid angle spectrometer of the beamline ID20 at the ESRF (Grenoble, France) dedicated to XRS studies [19, 20]. The pink beam from four U26 undulators was monochromatized by using a nitrogen cooled Si(111) monochromator and a Si (311) Channel Cut post-monochromator and then focused to a spot size of approximately 10 × 20 μm^2 (V × H) at the sample position with a mirror system in Kirkpatrick-Baez geometry. Measurements were performed by scanning the incident energy E_i so that the energy loss [E_f - E_i] matches the core-electron excitation of interest, in this case C and F K-edge. XRS data were collected in the vertical scattering plane using 36 spherically bent Si(660) analyzer crystals at the final energy E_f of 9.8 KeV and using 3 pixelated Maxipix detectors [28]. The overall energy resolution was 0.7 eV and the mean momentum transfer was 3.2 ± 0.3 Å^{-1}. All the samples were handled in air, ground into fine powder and pressed in an *ad-hoc* grooved flat Aluminium sample holder. The sample holder was placed on the goniometer stage at an incident beam angle of 10 degrees. All measurements were collected at room temperature and checked for consistency. The inelastic data were integrated over appropriated Region Of Interest (ROIs), averaged over the 36 crystals and treated with the

XRS tools program package [29]. A background accounting for the valence Compton profile was subtracted following the procedure described in [29]. Finally normalization over the area across the edge was applied. XRS spectra are presented in energy loss scale.

2.3. Computational details

All the calculations were performed within the *ab-initio* framework of the density functional theory using the pseudopotential and plane waves method, as implemented in the VASP code [30, 31]. The parameters of the calculation are similar to those previously used in Ref [13, 14], with the van der Waals corrections to the total energy taken into account at the DFT level using the so-called Grimme's D2 method [32]. The two 2s and two 2p outermost valence electrons of C and the two 2s and five 2p outermost valence electrons of F were dealt with explicitly in the calculations, while the rest of the electrons were considered frozen at the core. A projector augmented wave scheme was used [33,34] with a kinetic-energy cutoff in the plane waves expansions of 600 eV whereas for the integration over the Brillouin zone 15×15×5 Monkhorst−Pack grids were used. All these calculations correspond to hydrostatic pressures spanning the region of interest and zero temperature, with the small effect of the zero point energy neglected. The analysis of the electron localization function (ELF) was performed once electronic self-consistency was achieved and has provided very useful information on the bonding features for the studied materials. ELF was calculated from the valence electronic density obtained within the pseudopotential scheme implemented in VASP and the results were visualized using the VESTA 3.4.3 software and Jmol Visualization tool [35, 36]. The net atomic charges (NAC) were also calculated by means of the DDEC6 code [37, 38] (the frozen core electrons were included in the charge analysis). We have also carried out calculations of the core level binding energies for the C-1s and F-1s core state, including final-state core hole effects (core-level relaxation energy), which involve the recalculation of the Kohn-Sham eigenvalues for the core states for the chosen atom using a half core-hole [39].

The C-1s and F-1s energy values are referred to the electrostatic potential at vacuum. The simulation periodic cell corresponds to a slab of material made up of a large enough number of layers (so as to recover bulk properties in the central layers of the slab) plus a large enough vacuum region between the periodic images.

3. Results and discussion

3.1 PDF analysis

A direct analysis of the Real Space data is carried out for the three C_4F, C_2F and C_1F samples together with pristine powder graphite, for both X-ray and neutron diffraction data. The results are listed in Table 1. In Fig. 1 X-ray data in both reciprocal (left panel) and direct space (right panel) are plotted while the reference simulated models for the considered structures are sketched in Fig. 2 and described in Ref [13, 14]. Neutron data are reported in the SI file.

XRD data in reciprocal space clearly evidence the presence of the (002) pure graphite reflection at $Q \sim 1.9$ Å^{-1} in all the samples, broader in C_4F while sharp and well-defined in C_2F and CF samples.

X-ray data in direct space show one single oscillation in the low r region of the $G(r)$ of C_4F, with the first shell distances centred at 1.44 Å (see Fig. 1 and Table 1 for esd). This value is in fair agreement with the DFT model a) in Fig. 2 and discussed in [14] that predicts three first short distances $C-C_{short} = 1.40$ Å, $C-F = 1.46$ Å and $C-C_{long} = 1.50$ Å, whose weighted average is about 1.46 Å. It is to note that these three distances cannot be resolved within the experimental resolution of the neutron and even synchrotron X-ray PDF data. The overestimation of the overall first short distances in the DFT model can be interpreted as an overestimation of the presence of the F atoms in the structure, with respect to the nominal fraction F/C = 0.25.
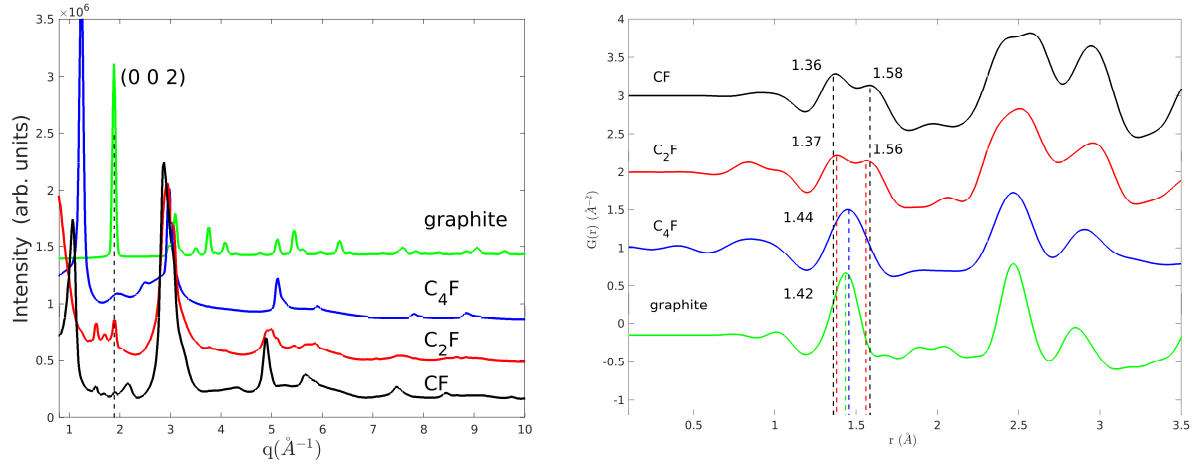
Figure 1. *XRD patterns in the q-range [0.8-10] Å^{-1} (left panel) and corresponding PDFs of graphite (green), C$_4$F (blue), C$_2$F (red), and CF (black) samples plotted up to 3.5 Å (right panel) collected at the ID15A beamline of the ESRF, using λ=0.18971 Å.*

(a)   (b1)   (b2)   (c)
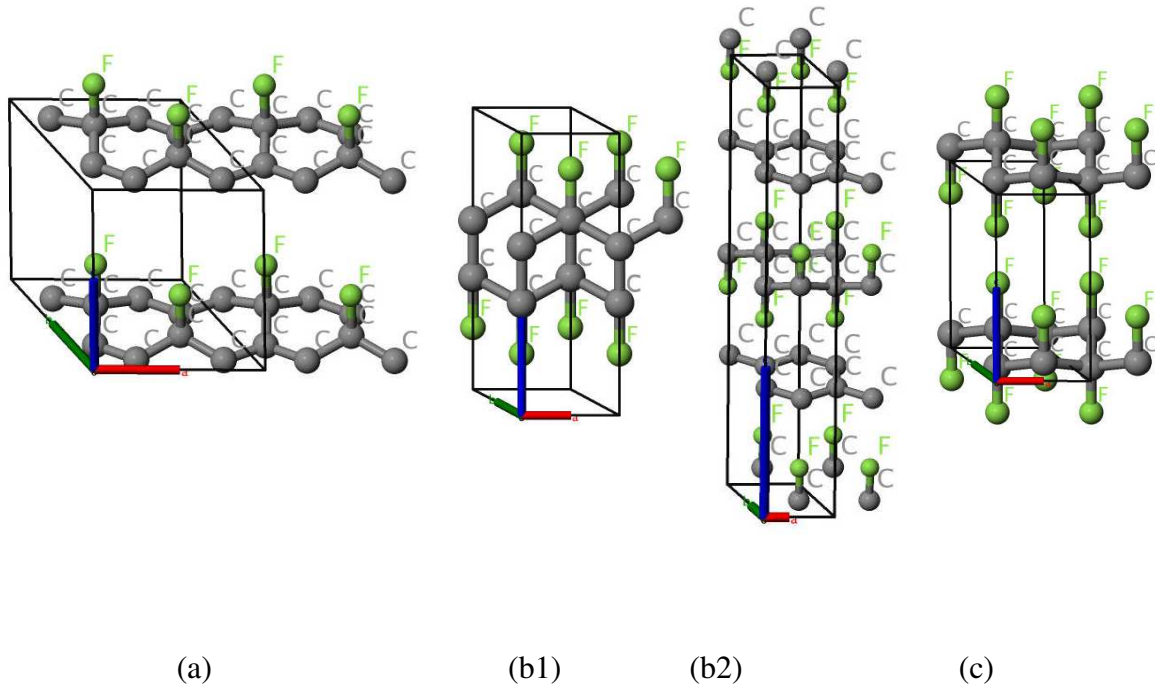
Figure 2: *Crystal structures of graphite fluorides for different fluorination percentages:*
(a) 25% - C$_4$F [14]; (b1 and b2) 50% - C$_2$F (sp^3) and C$_2$F (sp^2-sp^3), respectively [13];
(c) 100% - CF [40].

|	PDF calculation / Å	Observed distances / Å		Observed distances / Å	
		from X-ray PDFs		from neutron PDFs	
graphite		1.425 ± 0.003		1.417 ± 0.005	
C₄F	1.40, 1.46 and 1.50 (model a)	1.438 ± 0.006		1.432 ± 0.005	
C₂F	1.37 and 1.56 (model b1)	1.375 ± 0.003	1.562 ± 0.003	1.50 ± 0.01	
CF	1.38 and 1.57 (model c)	1.361 ± 0.002	1.574 ± 0.002	1.330 ± 0.005	1.570 ± 0.005

Table 1. *First neighbours distances in the three fluorinated compounds, C_4F, C_2F and CF as observed in the experimental X-ray and neutron PDF data. The estimated standard deviations of the experimentally observed distances are derived from Gaussian fits of the G(r) curves.*

For the C_2F sample, experimental data show two distances in the low r region of the PDF at 1.37 Å and 1.56 Å (see Figure 1, right panel), which agree very well with the distances C-F = 1.37 Å and C-C =1.56 Å predicted by the DFT model firstly proposed by Sato et al. [10] (model b1 in Fig. 2) and recently discussed in [13]. In general, short distances at around 1.38 Å corresponding to C-F bonds may be enhanced by the presence of a larger number of dangling bonds at the edge of coherent (graphitic or not) domains. So, the smaller are the domains, *e.g.* in presence of a more disordered structure, the larger is the number of such C-F bonds. Therefore, this peak would appear stronger in the PDF. It should be noticed that the agreement with the model proposed by Han et al. [15] and by Pischedda et al. [13] (model b2 in Fig. 2) is poorer, i.e. with the distance at 3.2 Å not reproduced in the experimental data. Moreover, both the models (b1 and b2 in Fig. 2) fail to reproduce satisfactorily the data above 5.8 Å. Data suggests that we are in presence of fragmented nanostructured domains of the structural models.

Similarly, in the C_1F sample, both X-ray and neutron data (see Table 1) show two distances in the low r region of the PDF, at 1.36 Å and 1.58 Å (see Fig. 1, right panel), which are in good agreement with the distances predicted by the DFT calculated model [40] (model c in Fig. 2),

i.e. C-F = 1.38 Å and C-C =1.57 Å. In this case, experimental data also seem to agree on second and third coordination shells. C_1F being the compound with the highest F/C ratio (x= 1), the proposed theoretical model is close to the observation.

To better understand the character of the C-C and C-F chemical bonds we report in Fig. 3 a theoretical study of the projected ELF along the C-F and C-C bonds at 25%-F coverage (C_4F, model a in Fig.2) and 100%-F coverage (CF, model c in Fig.2).
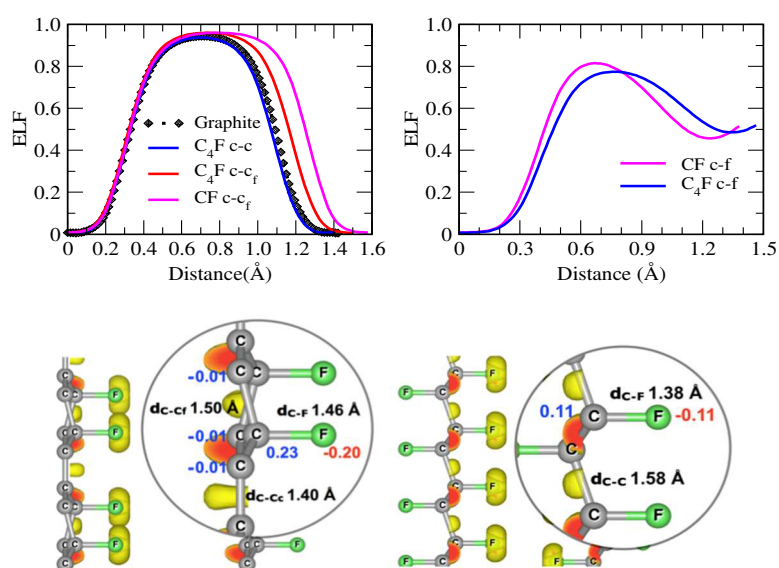
Figure 3*: (top) ELF profiles in function of the distance between the two bonded atoms (left panel: C-C and C-C$_F$. Right panel: C-F). A value of one indicates a high localization of electrons. For covalent bonds the valence electrons are localized between the two bonded atoms whereas for ionic bonds the valence electrons are localized near the anions. (bottom) Net atomic charges (NAC) at 25%-F coverage (left image) and 100%-F coverage (right image). A blue color is used to report the value of NAC on the C atoms whereas red indicates the NAC on the F atoms.*

The ELF profiles depicted in Fig. 3 (top) reveal the formation of strong covalent C-C bonds (top left graph) and weakened covalent C-F bonds (top right graph). The large difference in electronegativity of C and F results in a partially ionic character for the C-F bonds and, at 25% F coverage, brings a charge transfer to the middle of the C-C bond and to the F atom. As

the fluorine coverage ratio increases, more carbon atoms become coordinated with fluorine atoms and this reduces the charge transfer from carbon to fluorine. NAC on the C and F atoms are shown in Fig. 3 (bottom panel) along with the length of the bonds; a NAC close to zero indicates a covalent sharing of electrons between the atoms. Both the results clearly point out the influence of the electronegativity of F in the bond length of C-F and of $C-C_F$, where one of the C atoms bonds to a fluorine atom. As it can be seen from Table 2, when carbon atoms are not connected to a fluorine atom, the C-C bond length is close to the value of 1.42 Å for graphite. The theoretical results for the bond lengths are in good agreement with the first distances from experimental PDF.

	Bond length (Å)		
Fluorination (%)	**$C-C_F$**	**$C-C_c$**	**C-F**
0		1.422	
25 (model a)	1.504	1.399	1.464
50 (model b1)	1.561	1.552	1.376
50 (model b2)	1.538	1.455	1.383
100 (model c)	1.578		1.380

Table 2: *DFT results for the bond lengths versus fluorine coverage for C_xF compounds. Distances are given in Å. $C-C_F$ is the bond length between two carbon atoms where one carbon atom is bound to a fluorine atom, whereas $C-C_c$ is the bond length between two carbon atoms none of them bound to fluorine, and C-F is the length of the bond between one carbon and one fluorine atom.*

3.2 X-ray Raman scattering data

a)   *b)*
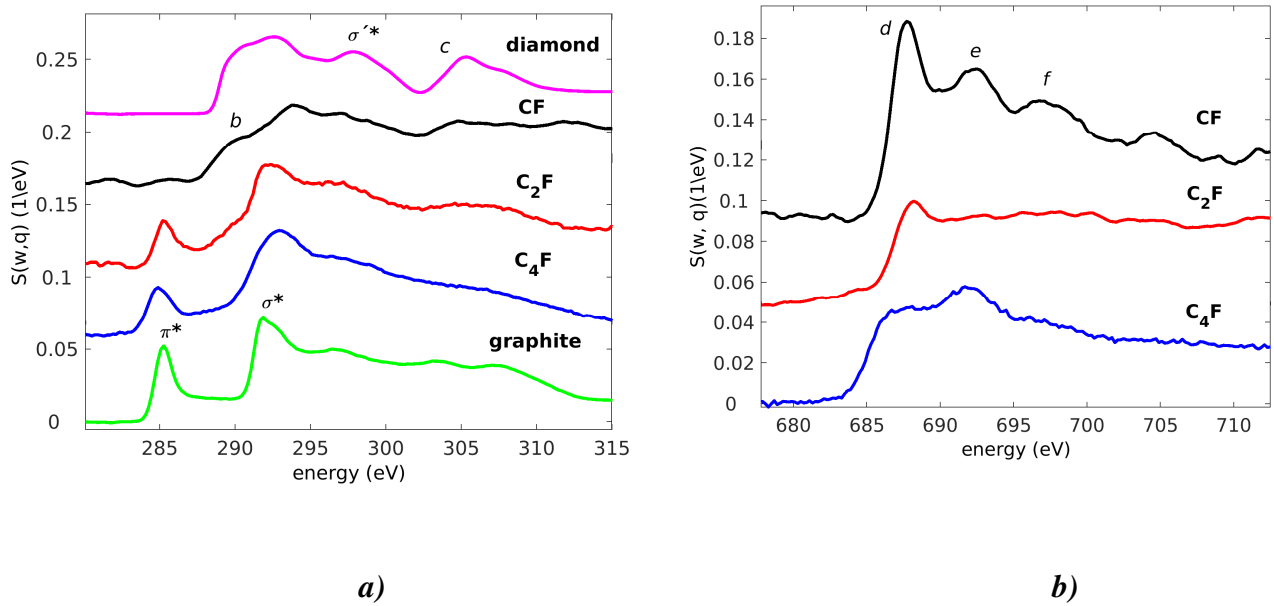
Figure 4. (a) *XRS spectra at the Carbon K edge of graphite fluorides at different fluorination degree. From the bottom to the top: in green graphite, in blue C_4F, in red C_2F, in black CF, in pink diamond.* **(b)** *XRS spectra at the Fluorine K-edge of graphite fluorides at different fluorination degree. From the bottom to the top: in blue C_4F, in red C_2F, in black CF.*

XRS spectra at the energy loss corresponding to the C K-edge and F K-edge for C_4F, C_2F and CF are shown in Fig. 4a and 4b respectively. The features at the C-K edge will be discussed first. Graphite and diamond powder have been measured as a reference and the experimental data are in good agreement with previous soft-XAS and EELS measurements [41, 42]. In graphite, the main features at the C 1s absorption edge are associated to the transitions of the C 1s electron of the empty π and σ states in the conduction band. These states, indicated as π* and σ*, come from the C $\pi 2p_z$ orbitals oriented perpendicular to the carbon plane and the sp^2 hybridized C $2s, 2p_{x,y}$ oriented in the carbon plane respectively. Therefore these are a clear indication of the C sp^2 hybridization that gives the trigonal C coordination within the graphene plane. In the graphite spectrum, the π* resonance is well defined at an energy of 285 eV, whereas the σ* band emerges at ~291 eV. The excitonic contribution expected at the edge onset [43] cannot be clearly distinguished from the σ* band itself because of the experimental resolution, both these features merging in one unique asymmetrical peak. The broader features extending above the threshold are attributed to core electron transitions to the empty σ electronic states in the conduction band associated to the interaction of carbon rings within

the plane [41]. In the case of diamond, the σ* band is broader, with an onset energy of ~289 eV. In this case, the sharp excitonic contribution is distinguishable at the edge onset. In addition, the feature c emerges at ~ 305 eV. It originates from a large intensity dip at 302 eV due to a second absolute gap in the diamond band structure [44]. Globally, the shape of the σ* band (including the features indicated as σ*, σ*' and c in Fig. 4a) is a fingerprint of the C sp^3 hybridization in diamond.

Notable changes are observed when comparing the XRS spectra of C_xF (x=4,2,1) with those of the C references. Graphite fluoride data are all characterized by a broadening of the bands and an up-shift of the σ* maximum. For C_4F, the compound that exhibits the lowest fluorination degree, the XRS spectrum maintains the same features of the graphite's one. As the F content increases from C_4F to CF, the π* peak gets broader and broader and it appears progressively depleted. In CF it shows up as a very weak bump but it is still present, indicating that, even at the highest fluorine content, the sample contains some double bonds due to incomplete fluorination. An additional resonance peak at ~ 289 eV, indicated as *b* in Fig 4a, can be observed at higher degree of F (x=2,1), together with a progressive change in the global shape of the σ* band, that approaches the one of diamond. Upon fluorination, F atoms bond to the carbon plane through the C $2p_z$ orbital and the carbon plane corrugates. This confirms that the chemical bonding between carbon atoms in highly graphite fluorides is mainly due to covalent σ bonds. It is noteworthy noticing that the features are globally ill-defined, most likely because of increased disorder and probable coexistence of several phases.

The XRS spectra at the F K-edge are reported in Fig. 4b. The features here are given by the F 1s electron transitions to the unoccupied electron states in the conduction band. The edge has an onset at around 685 eV and it is basically flat above 710 eV. We can distinguish three main bands: *d* from 686 to 688.5 eV, *e* at 693 eV and *f* from 695 to 700 eV. The edge onset shifts towards higher energy for the C_xF compounds with higher degree of fluorination (x=1,2). Moreover the relative intensity between *d* and *f* changes varying the stoichiometry: in C_4F *e* is more intense than *d*, in C_2F and CF this behavior is inverted, like for covalent C-F bonding in fluorobenzine [45]. This contrast is related to the number of free available electron states in the conduction band and gets modulated by the spatial orientation of the C-F bonds. Data of C_4F do not correlate well with NEXAFS spectra of ionic C_6F [46], even though a precise comparison cannot be done as the samples were synthetized differently and XRS provides a powder averaged signal with high sensitivity to the core.

For both the edges, the agreement with previous soft X-ray NEXAFS characterization of the same C_xF (x=4,2,1) compounds [12] is very good: the global spectral shape, energy position

and relative intensity of the peaks in the two datasets show an excellent match. However it should be noticed that, for all the stoichiometries and in particular at high F content, the fine structure of the XRS spectra is less clear and defined than the NEXAFS data. The first reason must be associated to the different energy resolution of the employed techniques: ~ 700meV (XRS) vs ~100 meV (NEXAFS). In addition, the sample depth probed by the two techniques is very different: few nm for the soft X-ray NEXAFS measurements [12] vs hundreds of μm of XRS. XRS data suggests that in the bulk the F atoms do not show a homogenous local atomic environment and coordination as at the surface.

In order to interpret the binding energies of the core levels measured by XRS, these were calculated for the C1s and F1s core states in the final state approximation. We compared the binding energies of the C1s core levels for C_4F and C_2F to those of C bonded only to C or F atoms. The calculated values of the binding energies from graphite (0% fluorination) to C_1F (100% fluorination) are given in Table 3.

| Material	Core hole level site	DFT calculation (eV)
C_1F	C1s	285.9
	F1s	689.0
C_2F (sp^3)	C1s (C)	284.6
	C1s (F)	285.8
	F1s	688.9
C_4F	C1s (C)	285.5
	C1s (F)	286.9
	F1s	687.0
C-graphite	C1s	285.4

Table 3: *Core Level Energies obtained from the DFT calculations.*

From these results we can see that in compounds in which the C atoms are bonded only to other C atoms, the C-1s values are similar to the ones obtained for graphite, however when the C atoms are attached to fluorine the energy value is higher.

The presence of the electronegative F atoms in the nearest surroundings of the C atoms causes some electron transfer from C towards F; therefore the effective positive charge on C

increases as well as the C-1s electron binding energy. This explains the progressive up-shift of the edge onset upon fluorination, particularly evident in highly graphite fluorides like CF. The results appear in good agreement with the reported binding energies measured by XRS and with the often reported values for the graphite core level [47]. C_2F compound is the one that shows the poorest agreement with the structural models proposed (models b1 and b2 in Fig. 2) and used for DFT calculations. Moreover both diffraction and XRS data indicate that the structural model for C_4F (model a in Fig. 2) tends to overestimate the F content. This may explain the slight discrepancies between theoretical and experimental values.
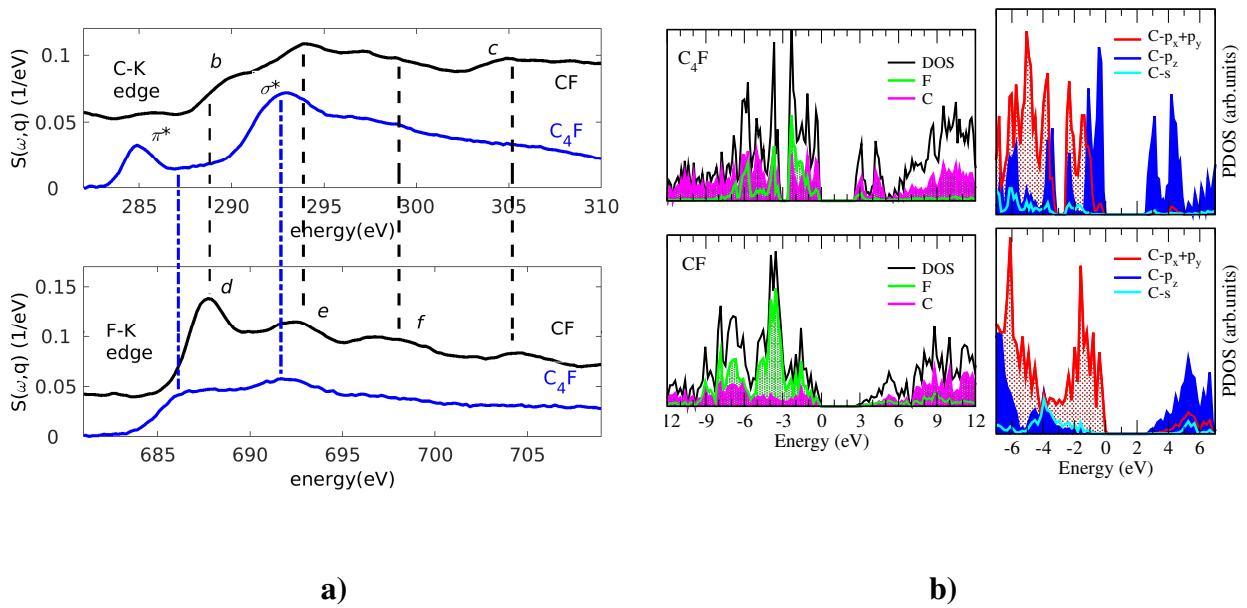
Figure 5: **a)** *Comparison between the XRS spectra at the C (top) and F (bottom) K-edge of CF (black curves) and C₄F (blue curves). The spectra are aligned in energy using the energy separation ΔE (F 1s –C1s) equal to ~ 399 eV [10].* **b)** *DOS and PDOS for both C₄F and CF with a zoom of PDOS corresponding to C atoms from DFT calculations.*

Following the analysis procedure described in [12], C-1s and F-1s spectra were aligned in energy by taking into account the energy separation between the F-1s and C-1s core levels. A value of ΔE ~399 eV was used for both C_1F and C_4F [10]. The result is shown in Figure 5a. The fine structures of these two spectra are similar for features' number, shape and energy position, confirming that they are associated to the transition of C-1s and F-1s core electrons to the same set of final states, formed primarily by F-2p and C-2p states [12]. We can see a clear correlation between the main peaks in both CF and C₄F spectra. In particular, *d* becomes

more intense and up-shifts in energy as the feature *b* does, while increasing the fluorination content from C_4F to CF, both being associated to the out of plane C-F bonds in the structure [12,46].

In Figure 5(b) we present the calculated total density of states (DOS) for the cases of 25% fluorination (C_4F) and 100% fluorination (C_1F), together with the projected density of states (PDOS) for each C and F species and projections onto s, p_x, p_y and p_z orbitals of the C atoms. Therefore, the way the peaks in the PDOS overlap can shed light on the hybridization character in the compound, confirming the main covalent character of the C-F bonds (as discussed from the analysis of the ELF data). The comparison of the calculated PDOS at 25% and 100% fluorine coverage shows substantial differences at the top of the valence band and a bottom of the conduction bands, being the contribution of C-p_x+p_y and C-p_z orbitals quite different. At 25% coverage a prominent peak of C-p_z character is observed for non-fluorinated neighbouring C atoms at the edge of the valence (bonding states) and conduction band (antibonding states) edges indicating a π-type bond, whereas in the case of 100% coverage the loss of this peak is observed. A significant hybridization of C-p_z states and C-p_x+p_y orbitals is observed. These results confirm the experimental data.

4. Conclusions

In the present paper we show two new advanced methodologies to investigate graphite fluorides C_4F, C_2F and C_1F as function of the fluorine and the residual sp^2 carbon atom contents, making use of XRS data and of PDF-analysed diffraction data, supported by DFT simulations. Information about the character of the C-F bonding were extracted, as well as about the first neighbour distances, the C-C and C-F bond lengths and finally the nature of the final states for 1s core-electron excitations probed by XRS. Our diffraction data, both in reciprocal and direct space, indicate the presence of a graphitic phase in the graphite fluorides compounds with stoichiometry C_4F, C_2F and CF. The analysis of XRS data confirms the presence of a graphitic phase, even at the highest fluorine content. With respect to the models proposed in literature, our study shows evidence for structural disorder and most likely coexistence of different phases, e.g. graphitic ones at the core of the particles where the diffusion of fluorine during the fluorination process is limited. Such data are crucial to deeply understand and therefore to optimize and control the synthesis with the view of practical applications. In the field of electrochemistry or tribology, the presence of a C-sp^2 phase in the fluorocarbon matrix is believed to trigger an improvement in the material performances.

Acknowledgments

References

[1] T. Nakajima. *Fluorine-Carbon and Fluoride-Carbon Materials: Chemistry, Physics, and Applications*. CRC Press, 2001.

[2] J. Giraudet, C. Delabarre, K. Guerin, M. Dubois, F. Masin, A. Hamwi. Comparative performances for primary lithium batteries of some covalent and semi-covalent graphite fluorides. *J. Power Sources*. 158 (2006) 1365–1372. doi:10.1016/j.jpowsour.2005.10.020.

[3] A. Hamwi, K. Guérin, M. Dubois, Chapter 17 - Fluorine-intercalated graphite for lithium batteries, in: T. Nakajima, H. Groult (Eds.). *Fluorinated Materials for Energy Conversion*. Elsevier Science, Amsterdam, 2005: pp. 369–395. doi:10.1016/B978-008044472-7/50045-X.

[4] R. Yazami, A. Hamwi, K. Guerin, Y. Ozawa, M. Dubois, J. Giraudet, F. Masin. Fluorinated carbon nanofibres for high energy and high power densities primary lithium batteries. *Electrochem. Commun*. 9 (2007) 1850–1855. doi:10.1016/j.elecom.2007.04.013.

[5] P. Thomas, P. Bilas, A. Molza, L. Legras, J.L. Mansot, K. Guérin, M. Dubois, *Fluorinated Nanocarbons for Lubrication, in: New Fluorinated Carbons: Fundamentals and Applications*. Elsevier, 2017: pp. 325–360. doi:10.1016/B978-0-12-803479-8.00014-0.

[6] N. Nomède-Martyr, E. Disa, P. Thomas, L. Romana, J.-L. Mansot, M. Dubois, K. Guérin, W. Zhang, A. Hamwi. Tribological properties of fluorinated nanocarbons with different shape factors. *J. Fluorine Chem*. 144 (2012) 10–16. doi:10.1016/j.jfluchem.2012.08.008.

[7] H. Touhara, K. Kadono, Y. Fujii, N. Watanabe. On the Structure of Graphite Fluoride, *Z. Anorg. Allg. Chem*. 544 (1987) 7–20. doi:10.1002/zaac.19875440102.

[8] J. Giraudet, M. Dubois, K. Guérin, A. Hamwi, F. Masin. Solid state NMR studies of covalent graphite fluorides (CF)n and (C2F)n. *J. Phys. Chem. Solids*. 67 (2006) 1100–1105. doi:10.1016/j.jpcs.2006.01.030.

[9] J. Giraudet, M. Dubois, A. Hamwi, W.E.E. Stone, P. Pirotte, F. Masin. Solid-State NMR (^{19}F and ^{13}C) Study of Graphite Monofluoride (CF)$_n$: ^{19}F Spin–Lattice Magnetic Relaxation and ^{19}F/ ^{13}C Distance Determination by Hartmann–Hahn Cross Polarization. *J. Phys. Chem. B*. 109 (2005) 175–181. doi:10.1021/jp046833j.

[10] Y. Sato, K. Itoh, R. Hagiwara, T. Fukunaga, Y. Ito. Short-range structures of poly(dicarbon monofluoride) $(C_2F)_n$ and poly(carbon monofluoride) $(CF)_n$. *Carbon*. 42 (2004) 2897–2903. doi:10.1016/j.carbon.2004.06.042.

[11] M. Dubois, J. Giraudet, K. Guérin, A. Hamwi, Z. Fawal, P. Pirotte, F. Masin. EPR and Solid-State NMR Studies of Poly(dicarbon monofluoride) $(C_2F)_n$. *J. Phys. Chem. B*. 110 (2006) 11800–11808. doi:10.1021/jp061291m.

[12] Y. Ahmad, M. Dubois, K. Guérin, A. Hamwi, Z. Fawal, A.P. Kharitonov, A.V. Generalov, A.Y. Klyushin, K.A. Simonov, N.A. Vinogradov, I.A. Zhdanov, A.B. Preobrajenski, A.S. Vinogradov. NMR and NEXAFS Study of Various Graphite Fluorides. *J. Phys. Chem. C*. 117 (2013) 13564–13572. doi:10.1021/jp401579u.

[13] V. Pischedda, S. Radescu, M. Dubois, N. Batisse, F. Balima, C. Cavallari, L. Cardenas. Experimental and DFT high pressure study of fluorinated graphite $(C_2F)n$. *Carbon*. 114 (2017) 690–699. doi:10.1016/j.carbon.2016.12.051.

[14] V. Pischedda, S. Radescu, M. Dubois, C. Cavallari, N. Batisse, F. Balima. Fluorine-graphite intercalation compound $(C_4F)_n$ at high pressure: Experimental and theoretical study. *Carbon*. 127 (2018) 384–391. doi:10.1016/j.carbon.2017.10.094.

[15] S.S. Han, T.H. Yu, B.V. Merinov, A.C.T. van Duin, R. Yazami, W.A. Goddard. Unraveling Structural Models of Graphite Fluorides by Density Functional Theory Calculations. *Chem. Mater*. 22 (2010) 2142–2154. doi:10.1021/cm903760t.

[16] J. Giraudet, M. Dubois, K. Guérin, C. Delabarre, A. Hamwi, F. Masin. Solid-state NMR study of the post-fluorination of $(C_{2.5}F)_n$ fluorine-GIC. *J. Phys. Chem. B*. 111 (2007) 14143–14151. doi:10.1021/jp076170g.

[17] T. Suzuki, X-Ray Raman Scattering Experiment. I. *J. Phys. Soc. Jpn*. 22 (1967) 1139–1150. doi:10.1143/JPSJ.22.1139.

[18] T. Suzuki, T. Kishimoto, T. Kaji, T. Suzuki. X-Ray Raman Scattering. II. Experiment with Cr Kα Radiation. *J. Phys. Soc. Jpn*. 29 (1970) 730–736. doi:10.1143/JPSJ.29.730.

[19] S. Huotari, C.J. Sahle, C. Henriquet, A. Al-Zein, K. Martel, L. Simonelli, R. Verbeni, H. Gonzalez, M.-C. Lagier, C. Ponchut, M. Moretti Sala, M. Krisch, G. Monaco. A large-solid-angle X-ray Raman scattering spectrometer at ID20 of the European Synchrotron Radiation Facility. *J. Synchrotron Rad.* 24 (2017) 521–530. doi:10.1107/S1600577516020579.

[20] S. Huotari, T. Pylkkänen, J.A. Soininen, J.J. Kas, K. Hämäläinen, G. Monaco. X-ray-Raman-scattering-based EXAFS beyond the dipole limit. *J. Synchrotron Rad.* 19 (2012) 106–113. doi:10.1107/S0909049511039422.

[21] T. Egami, S.J.L. Billinge. *Underneath the Bragg Peaks: Structural Analysis of Complex Materials*. Elsevier, 2003.

[22] G. Ashiotis, A. Deschildre, Z. Nawaz, J.P. Wright, D. Karkoulis, F.E. Picca, J. Kieffer. The fast azimuthal integration Python library: pyFAI. *J. Appl. Cryst*. 48 (2015) 510–519. doi:10.1107/S1600576715004306.

[23] P. Juhás, T. Davis, C.L. Farrow, S.J.L. Billinge. PDFgetX3: a rapid and highly automatable program for processing powder diffraction data into total scattering pair distribution functions. *J. Appl. Cryst*. 46 (2013) 560–566. doi:10.1107/S0021889813005190.

[24] C. Cavallari, M. Brunelli, M. Dubois, H.E. Fischer, V. Pischedda, S. Radescu. Neutron powder diffraction study of fluorinated graphites. (2018). doi:10.5291/ILL-DATA.6-06-479.

[25] H.E. Fischer, G.J. Cuello, P. Palleau, D. Feltin, A.C. Barnes, Y.S. Badyal, J.M. Simonson. D4c: A very high precision diffractometer for disordered materials. *Appl Phys A*. 74 (2002) s160–s162. doi:10.1007/s003390101087.

[26] H.E. Fischer, A.C. Barnes, P.S. Salmon. Neutron and x-ray diffraction studies of liquids and glasses. *Reports on Progress in Physics*. 69 (2006) 233–299. doi:10.1088/0034-4885/69/1/R05.

[27] H.M. A, M.R. L, Z. P, CORRECT: *A correction program for neutron diffraction data, NFL*, Uppsala University, 1996.

[28] C. Ponchut, J.M. Rigal, J. Clément, E. Papillon, A. Homs, S. Petitdemange. MAXIPIX, a fast readout photon-counting X-ray area detector for synchrotron applications. *J. Inst*. 6 (2011) C01069. doi:10.1088/1748-0221/6/01/C01069.

[29] C.J. Sahle, A. Mirone, J. Niskanen, J. Inkinen, M. Krisch, S. Huotari. Planning, performing and analyzing X-ray Raman scattering experiments. *J. Synchrotron Rad*. 22 (2015) 400–409. doi:10.1107/S1600577514027581.

[30] G. Kresse, J. Furthmüller. Efficiency of ab-initio total energy calculations for metals and semiconductors using a plane-wave basis set. *Computational Materials Science*. 6 (1996) 15–50. doi:10.1016/0927-0256(96)00008-0.

[31] G. Kresse, J. Furthmüller. Efficient iterative schemes for *ab initio* total-energy calculations using a plane-wave basis set. *Phys. Rev. B*. 54 (1996) 11169–11186. doi:10.1103/PhysRevB.54.11169.

[32] J.P. Perdew, A. Ruzsinszky, G.I. Csonka, O.A. Vydrov, G.E. Scuseria, L.A. Constantin, X. Zhou, K. Burke. Restoring the Density-Gradient Expansion for Exchange in Solids and Surfaces. *Phys. Rev. Lett*. 100 (2008). doi:10.1103/PhysRevLett.100.136406.

[33] J.P. Perdew, K. Burke, M. Ernzerhof. Generalized Gradient Approximation Made Simple. *Phys. Rev. Lett*. 77 (1996) 3865–3868. doi:10.1103/PhysRevLett.77.3865.

[34] S. Grimme, J. Antony, S. Ehrlich, H. Krieg. A consistent and accurate ab initio parametrization of density functional dispersion correction (DFT-D) for the 94 elements H-Pu. *J. Chem. Phys*. 132 (2010) 154104. doi:10.1063/1.3382344.

[35] K. Momma, F. Izumi. VESTA 3 for three-dimensional visualization of crystal, volumetric and morphology data. *J. Appl. Cryst*. 44 (2011) 1272–1276. doi:10.1107/S0021889811038970.

[36] Jmol: an open-source Java viewer for chemical structures in 3D. http://jmol.sourceforge.net/index.en.html

[37] T.A. Manz, N.G. Limas. Introducing DDEC6 atomic population analysis: part 1. Charge partitioning theory and methodology. *RSC Adv*. 6 (2016) 47771–47801. doi:10.1039/C6RA04656H.

[38] N.G. Limas, T.A. Manz. Introducing DDEC6 atomic population analysis: part 2. Computed results for a wide range of periodic and nonperiodic materials. *RSC Adv*. 6 (2016) 45727–45747. doi:10.1039/C6RA05507A.

[39] L. Köhler, G. Kresse. Density functional study of CO on Rh(111). *Phys. Rev. B*. 70 (2004) 165405. doi:10.1103/PhysRevB.70.165405.

[40] J.-C. Charlier, X. Gonze, J.-P. Michenaud. First-principles study of graphite monofluoride (CF)n. *Phys. Rev. B*. 47 (1993) 16162–16168. doi:10.1103/PhysRevB.47.16162.

[41] P.E. Batson, Carbon 1s near-edge-absorption fine structure in graphite. *Phys. Rev. B*. 48 (1993) 2608–2610. doi:10.1103/PhysRevB.48.2608.

[42] Y. Ma, N. Wassdahl, P. Skytt, J. Guo, J. Nordgren, P.D. Johnson, J.-E. Rubensson, T. Boske, W. Eberhardt, S.D. Kevan. Soft-x-ray resonant inelastic scattering at the C K edge of diamond. *Phys. Rev. Lett*. 69 (1992) 2598–2601. doi:10.1103/PhysRevLett.69.2598.

[43] P.A. Brühwiler, A.J. Maxwell, C. Puglia, A. Nilsson, S. Andersson, N. Mårtensson. π∗and σ∗ Excitons in C 1s Absorption of Graphite. *Phys. Rev. Lett*. 74 (1995) 614–617. doi:10.1103/PhysRevLett.74.614.

[44] A. Gloter, A. Douiri, M. Tencé, C. Colliex. Improving energy resolution of EELS spectra: an alternative to the monochromator solution. *Ultramicroscopy*. 96 (2003) 385–400. doi:10.1016/S0304-3991(03)00103-7.

[45] A.P. Hitchcock, P. Fischer, A. Gedanken, M.B. Robin. Antibonding .sigma.* valence MOs in the inner-shell and outer-shell spectra of the fluorobenzenes. *J. Phys. Chem.* 91 (1987) 531–540. doi:10.1021/j100287a009.

[46] K. Seki et al. High-Energy Spectroscopic Studies of the Electronic Structures of Organic Systems Formed from Carbon and Fluorine by UPS, Vacuum-UV Optical Spectroscopy, and NEXAFS: Poly(hexafluoro-1,3-butadiene) $[C(CF_3)=C(CF_3)]_n$, Fluorinated Graphites (CF, C_2F, and C_6F), Perfluoroalkanes n-$C_n F_{2n+2}$, Poly(tetrafluoroethylene) $(CF_2)_n$, and Fluorinated Fullerenes ($C_{60}F_x$ and $C_{70}F_x$). *Molecular Crystals and Liquid Crystals Science and Technology. Section A. Molecular Crystals and Liquid Crystals.* 355 (2006) 247–274. doi:10.1080/10587250108023664.

[47] T. Susi, T. Pichler, P. Ayala. X-ray photoelectron spectroscopy of graphitic carbon nanomaterials doped with heteroatoms. *Beilstein Journal of Nanotechnology.* 6 (2015) 177–192. doi:10.3762/bjnano.6.17.